

On-Line Safe Flight Envelope Determination for Impaired Aircraft

Thomas Lombaerts, Stefan Schuet, Diana Acosta and John Kaneshige

Abstract The design and simulation of an on-line algorithm which estimates the safe maneuvering envelope of aircraft is discussed in this paper. The trim envelope is estimated using probabilistic methods and efficient high-fidelity model based computations of attainable equilibrium sets. From this trim envelope, a robust reachability analysis provides the maneuverability limitations of the aircraft through an optimal control formulation. Both envelope limits are presented to the flight crew on the primary flight display. In the results section, scenarios are considered where this adaptive algorithm is capable of computing online changes to the maneuvering envelope due to impairment. Furthermore, corresponding updates to display features on the primary flight display are provided to potentially inform the flight crew of safety critical envelope alterations caused by the impairment.

1 Introduction

In all transportation systems, but especially in civil aviation, safety is of paramount importance. Many developments focus on improving safety levels and reducing the risks of life threatening failures. In a recent study by the Commercial Aviation Safety Team (CAST) and the International Civil Aviation Organization (ICAO), it can be observed that loss of control in flight (LOC-I) is the most frequent primary accident cause. This study is based on a statistical analysis of aircraft accidents be-

Thomas Lombaerts
German Aerospace Center (DLR), Robotics and Mechatronics Center, Institute of System Dynamics and Control, Oberpfaffenhofen, D-82234 Weßling, Germany, e-mail: Thomas.Lombaerts@dlr.de

Stefan Schuet · Diana Acosta · John Kaneshige
NASA Ames Research Center, Intelligent Systems Division, CA 94035 Moffett Field, USA e-mail: Stefan.R.Schuet@nasa.gov e-mail: Diana.M.Acosta@nasa.gov e-mail: John.T.Kaneshige@nasa.gov

tween 2002 and 2011, and indicates that this category accounts for as much as 23% of all fatal aircraft accidents and involves most fatalities[1]. LOC-I can have various causes, occurring individually or in combination, such as a system malfunction, atmospheric disturbances (e.g. turbulence or icing), and loss of situational awareness by the crew. An important aspect during operations under system malfunction or atmospheric disturbance is that the crew needs to maintain awareness through possibly time changing degradation of aircraft performance characteristics. The CAST established a specialized international safety analysis team to study the apparent growing trend in loss of Airplane State Awareness (ASA) by the flight crew. This team has produced recommended safety enhancements that include research to develop and implement technologies for enhancing flight crew awareness of airplane energy state (SE 207)[2]. The approach developed in this paper focuses on increasing awareness of the boundaries of the safe flight envelope over which the pilot can maneuver without losing control over the plane. These boundaries can be updated based on possibly time changing flow of information regarding the aircraft state.

A variety of methods conforming to this concept have been investigated in previous studies. The most straightforward methods include wind tunnel testing, flight test experiments and high-fidelity model-based computation of attainable equilibrium sets or achievable trim points[23], possibly with bifurcation analysis [7] or a vortex lattice algorithm combined with an extended Kalman filter[16]. More complex methods include formulating flight envelope estimation as a reachability problem and solving this with level set methods and Hamilton-Jacobi equations [15], possibly with time scale separation [5] or semi-Lagrangian level sets [19]. Alternative methods rely on linearization and region of attraction analysis [20], determining controllability/maneuverability limits in a quaternion-based control architecture[3] or robustness analysis for determination of reliable flight regimes [22]. An approach suggested by Boeing uses Control-Centric Modeling, dynamic flexible structure and load models [24]. In the frequency domain, stability margins can be estimated in real time via nonparametric system identification [8]. More focused techniques inspired by flight dynamics exist as well, such as determining the minimum lateral control speed[6]. In this approach, the trim envelope is estimated through efficient high-fidelity model-based computations of attainable equilibrium sets based on aerodynamic coefficient identification from air data, inertial and GPS measurements. The corresponding maneuverability limitations of the aircraft are then determined through a robust reachability analysis (relative to the trim envelope) through an optimal control formulation and based on the principle of time scale separation. The theoretical underpinnings covering the overall approach are available in previous publications[12, 21].

The structure of this paper is as follows. In Sec. 2, the estimation of the envelope boundaries is discussed. The method for presenting this information to the crew is elaborated in Sec. 3. Sec. 4 discusses some relevant application example scenarios. Conclusions and recommendations can be found in Sec. 5. Further related research based on the results presented here is described in Sec. 6.

2 Estimation of the envelope boundaries

The safe maneuvering envelope is a fundamental property of the aircraft's design and overall current state of health. By definition it determines the overall capability of the aircraft. If actively monitored in time, it may function as an early warning system as well as provide anticipatory guidance to help avoid loss of control. For example, automated planning tools may use it to help pilots land safely under emergency landing conditions[17], or when combined with a display it may result in overall better pilot awareness of the state of the aircraft. This can be particularly useful when an automation system switches off. Additionally, the physics-based maneuverability envelope can be analyzed separately from the control strategy, and knowledge of the envelope may for example unmask control limitations clouded by adaptive controllers, and even lower barriers to the introduction of more advanced unconventional control strategies[9]. For these reasons, improved methods for tracking aircraft maneuverability in real-time may effectively help pilots avoid inappropriate crew response and further prevent or recover aircraft from upset conditions. Generally, the maneuvering envelope is the set of safe aircraft state and control inputs. Unfortunately, because of the underlying nonlinear aircraft dynamics, it is challenging to calculate this set of states accurately and rapidly enough to provide the pilot or automation system with reliable information in a diverse and rapidly changing environment.

2.1 Mathematical model postulation and parameter identification

The aircraft model used for this simulator study is the nonlinear RCAM (Research Civil Aircraft Model) simulation model, which is representative of a large two-engine jet transport with general characteristics of a wide-body, conventional tail and low wing airplane configuration with twin turbofan engines located under the wings[14]. The physical dimensions are similar to an Airbus A300 aircraft, with flight characteristics representative of a large jet transport in landing configuration (flaps at 32.5 deg and gear down) at sea level. A selection of RCAM model data is provided in Table 1.

Table 1 Selection of parameter values for RCAM model

Constants	Aerodynamic Coefficients	Input Bounds
$S = 260 \text{ m}^2$ $m = 120 \times 10^3 \text{ kg}$ $g = 9.81 \text{ m/s}^2$ $\rho = 1.225 \text{ kg/m}^3$	$C_{D_0} = 0.1599$ $C_{D_\alpha} = 0.5035$ $C_{m_0} = -0.015$ $C_{D_{\alpha^2}} = 2.1175$ $C_{m_\alpha} = -2.15$ $C_{L_0} = 1.0656$ $C_{m_q} = -14.0$ $C_{L_\alpha} = 6.0723$ $C_{m_{\delta_e}} = -2.87$ $C_{Y_\beta} = -1$	$T \in [20546, 410920] \text{ N}$ $\alpha \in [0, 14.5] \text{ deg.}$ $\delta_e \in [-30.0, 20.0] \text{ deg.}$

Nonlinear aircraft dynamics with higher dimensions can be simplified by considering the principle of time scale separation[5]. The structure of time scale separation is analogous as applied for the fault tolerant control algorithm developed earlier[9]. The overview can be found in Fig. 1, which illustrates that a nine dimensional nonlinear problem is decoupled in three consecutive three dimensional optimization problems.

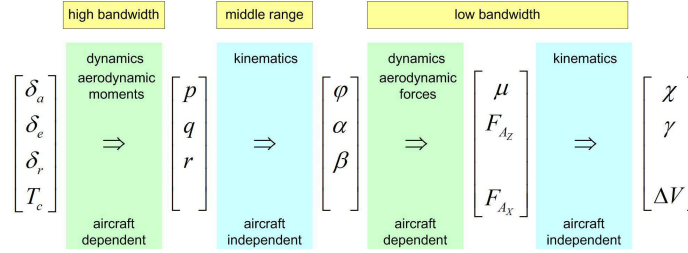


Fig. 1 Separation of dynamics over high bandwidth, middle range and low bandwidth

2.1.1 Model postulation

A nonlinear 3D aircraft example is considered. Main focus of this research is on the slow aircraft dynamics as specified in Fig. 1, involving the aerodynamic forces lift L , drag D and sideforce Y_{aero} . Also the pitching moment M , as part of the fast dynamics, has been included in the model but this moment can be considered separately from the aerodynamic forces, thanks to the principle of time scale separation, see Fig. 1. The acting forces on the aircraft are illustrated in Fig. 2 for a symmetric flight condition.

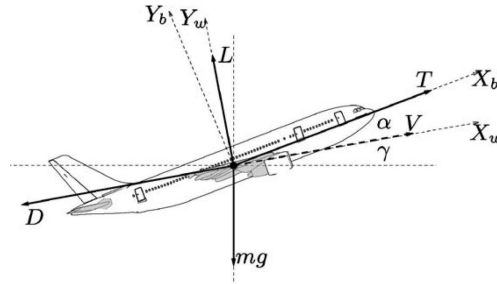


Fig. 2 Acting forces on the aircraft model, source: Lygeros[15]

For the complete 3D situation, the equations of motion are written as follows[9]:

$$F_{Ax} - W \sin \gamma = m\dot{V} \quad (1)$$

$$F_{Az} \cos \varphi + F_{Ay} \sin \varphi + W \cos \gamma = -mV\dot{\gamma} \quad (2)$$

Where the aerodynamic forces can be simplified assuming small aerodynamic angles α and β :

$$F_{Ax} = T \cos \beta \cos \alpha - D(V, \alpha) \approx T - D(V, \alpha) \quad (3)$$

$$F_{Az} = -T \sin \alpha - L(V, \alpha) \approx -L(V, \alpha) \quad (4)$$

$$F_{Ay} = -T \sin \beta \cos \alpha + Y_{\text{aero}}(V, \beta) \approx Y_{\text{aero}}(V, \beta) \quad (5)$$

with the following expansions for lift L , drag D and sideforce Y_{aero} :

$$D(V, \alpha) = \bar{q}S \left(C_{D_0} + C_{D_\alpha} \alpha + C_{D_{\alpha^2}} \alpha^2 \right) \quad (6)$$

$$L(V, \alpha) = \bar{q}S \left(C_{L_0} + C_{L_\alpha} \alpha \right) \quad (7)$$

$$Y_{\text{aero}}(V, \beta) = \bar{q}S \left(C_{Y_\beta} \beta \right) \quad (8)$$

where the dynamic pressure $\bar{q} = 1/2\rho V^2$.

The aircraft dynamics are combined in the following matrix structure:

$$\begin{bmatrix} \dot{V} \\ \dot{\gamma} \end{bmatrix} \approx \begin{bmatrix} -\frac{\rho S}{2m} V^2 C_{D_0} - g \sin \gamma \\ -\frac{g}{V} \cos \gamma \end{bmatrix} + \begin{bmatrix} 1 \\ 0 \end{bmatrix} \frac{T}{m} + \begin{bmatrix} -\frac{\rho S}{2m} V^2 \left(C_{D_\alpha} \alpha + C_{D_{\alpha^2}} \alpha^2 \right) \\ \frac{\rho S}{2m} V \left(C_{L_0} + C_{L_\alpha} \alpha \right) \cos \varphi \end{bmatrix} + \begin{bmatrix} 0 \\ -\frac{\rho S}{2m} V C_{Y_\beta} \beta \sin \varphi \end{bmatrix} \quad (9)$$

where thrust T and angle of attack α are treated as virtual inputs, based on the time scale separation principle as illustrated in Fig. 1. An affine matrix structure in the inputs is obtained by simplifying for small angles of attack α and sideslip β .

The pitching moment structure typically varies for every aircraft type. For this specific model, a model structure selection analysis[10, 9] has provided the following structure:

$$C_m = C_{m_0} + C_{m_\alpha} \alpha + C_{m_{\frac{q\bar{c}}{V}}} \frac{q\bar{c}}{V} + C_{m_{\delta_e}} \delta_e + C_{m_{i_h}} i_h + C_{m_T} \frac{T}{\bar{q}d_{\text{eng}}^2} \quad (10)$$

2.1.2 Parameter identification

In order to characterize the flight envelope of a particular aircraft, the as of yet undetermined aerodynamic coefficients need to be reconstructed using available sensor measurements. This is a necessary step, that essentially fits the above described dynamics model to any particular aircraft, or aircraft simulation of higher fidelity. An inertial sensor package, consisting of rate gyros and accelerometers, provides angular rates and accelerations as well as specific forces. It is assumed that a state estimation algorithm[13] is available, taking into account sensor disturbances (biases and/or noise), and compensating for them.

The forces in the body fixed reference frame are reconstructed from:

$$X_{\text{tot}} = mA_x \quad Y_{\text{tot}} = mA_y \quad Z_{\text{tot}} = mA_z \quad (11)$$

$$C_X = \frac{X}{\bar{q}S} = \frac{T - X_{\text{tot}}}{\bar{q}S} \quad C_Y = \frac{Y}{\bar{q}S} \quad C_Z = \frac{Z}{\bar{q}S} \quad (12)$$

where A_x , A_y and A_z are the specific forces as measured by the accelerometers. The force coefficients in the body fixed reference frame are then transformed to the aerodynamic reference frame using

$$\begin{pmatrix} -C_D \\ C_{Y_{\text{aero}}} \\ -C_L \end{pmatrix} = \begin{pmatrix} \cos \alpha & 0 & \sin \alpha \\ 0 & 1 & 0 \\ -\sin \alpha & 0 & \cos \alpha \end{pmatrix} \cdot \begin{pmatrix} \cos \beta & \sin \beta & 0 \\ -\sin \beta & \cos \beta & 0 \\ 0 & 0 & 1 \end{pmatrix} \cdot \begin{pmatrix} C_X \\ C_Y \\ C_Z \end{pmatrix}. \quad (13)$$

Finally, the pitching moment coefficient is reconstructed from the corresponding moment equation

$$C_m = \frac{M}{\bar{q}S\bar{c}} = \frac{\dot{q}I_{yy} + pr(I_{xx} - I_{zz}) + (p^2 - r^2)I_{xz}}{\bar{q}S\bar{c}}, \quad (14)$$

where I_{xx} , I_{yy} , I_{zz} , and I_{xz} are the components of the inertia matrix in the body axis, and where p , q , and r are respectively the roll, pitch, and yaw rate components of the body-axis angular velocity.

The above defined flight dynamics model provides the means through which one can assess the flight performance capability of the aircraft. However, it depends on a set of effective aerodynamic coefficients, which should be estimated from the combination of available sensor data and the known physical relationships between quantities specified by the model. The aerodynamic coefficient vector to be identified for the forces is defined as:

$$\mathbf{c} = [C_{D0}, C_{D\alpha}, C_{D_{\alpha^2}}, C_{L0}, C_{L\alpha}]^T,$$

and the moment coefficient vector is:

$$\mathbf{m} = [C_{m0}, C_{m\alpha}, C_{m_{\dot{q}}}, C_{m_{\delta_e}}, C_{m_{\delta_h}}, C_{m_T}]^T.$$

A specialized Bayesian probabilistic approach was developed to infer the unknown aerodynamic coefficients from the noisy sensor measurements and to quantify the estimation uncertainty; an overview of which is provided next. More information about the identification procedure, including results, can be found in Schuet et. al. [21].

A state measurement process $\mathbf{x}(k) = [V(k), \gamma(k)]$ is defined, which proceeds, for $k = 1, 2, \dots, m-1$, according to a midpoint-Euler discrete approximation:

$$\mathbf{x}(k+1) = \mathbf{x}(k) + h\mathbf{f}(\tilde{\mathbf{x}}, \mathbf{u}; \mathbf{c}) + \boldsymbol{\tau}(k), \quad (15)$$

where $\mathbf{f}(\mathbf{x}, \mathbf{u}; \mathbf{c})$ represents the continuous flight dynamics model (9), \mathbf{u} is the vector of known virtual inputs at time instance k ,

$$\mathbf{u}(k) = [T, \alpha, \beta]^T,$$

h is the time-sample resolution, $\tilde{\mathbf{x}} = [\mathbf{x}(k) + \mathbf{x}(k+1)]/2$ is the midpoint, and $\boldsymbol{\tau}(k) \sim \mathcal{N}(0, h\mathbf{S}^{-1})$ is the additive independent and identically distributed Gaussian measurement noise process. While the maneuverability model is linear in \mathbf{c} , it is still nonlinear in \mathbf{x} and \mathbf{u} , and the midpoint-Euler approximation enables better representation of the true nonlinear system, for negligible additional computational cost. The inverse covariance matrix \mathbf{S} is an important statistical parameter that characterizes the process noise $\boldsymbol{\tau}(k)$, which will also be estimated from the observed data.

In similar fashion, one can also define processes for the accelerometer measurements

$$\mathbf{x}_a(k) = \mathbf{A}_k \mathbf{c} + \boldsymbol{\tau}_a(k),$$

where \mathbf{A}_k is a matrix, depending on $\mathbf{u}(k)$, that implements the combination of (13) and (6)–(8). Finally, the moment measurement process is defined as

$$x_m(k) = \mathbf{M}_k \mathbf{m} + \tau_m(k),$$

where \mathbf{M}_k is a row vector implementing (10), that depends on the moment model input variables. Also, $\boldsymbol{\tau}_a$ and τ_m represent independent additive Gaussian measurement noise terms for the accelerometer and moment measurements, with associated inverse covariance matrix \mathbf{S}_a and scalar inverse variance S_m , respectively. Furthermore, the moment measurement process is independent of the dynamics and accelerometer measurement processes, and can therefore be treated by a separate inference process, that follows the same approach used to infer the aerodynamic force coefficients summarized next.

Focusing on the estimation of the force coefficient vector \mathbf{c} , the above measurement model equations and Gaussian noise distribution assumptions enable one to specify the multivariate probability density function (pdf) for the measured data given the model parameters

$$p(\mathbf{X}, \mathbf{X}_a | \mathbf{c}, \mathbf{S}, \mathbf{S}_a, \mathbf{U}), \quad (16)$$

where \mathbf{X} , \mathbf{X}_a , and \mathbf{U} represent matrices containing the entire history of state, accelerometer, and input data measurements, respectively. Through Bayes' Theorem, the *likelihood* pdf (16) can then be combined with appropriate prior information to determine the *posterior* pdf

$$p(\mathbf{c}, \mathbf{S}, \mathbf{S}_a | \mathbf{X}, \mathbf{X}_a, \mathbf{U}) \quad (17)$$

that specifies the probability density of the unknown parameter values \mathbf{c} and inverse measurement noise covariance matrices, given all of the observed data and prior information. The optimal parameter estimate is then found by solving

$$\text{maximize } p(\mathbf{c}, \mathbf{S}, \mathbf{S}_a | \mathbf{X}, \mathbf{X}_a, \mathbf{U}) \quad (18)$$

with respect to the unknown aerodynamics coefficients \mathbf{c} and inverse covariance matrix terms \mathbf{S} and \mathbf{S}_a .

With the modeling and additive noise assumptions used in the derivation, the posterior pdf (17) is log-concave in any one of the variables \mathbf{c} , \mathbf{S} , or \mathbf{S}_a when the other two variables are held fixed. This enables the efficient computation of a local optimal estimate using a block coordinate descent method to break the solution process into steps that require solving simple convex optimization problems. Furthermore, the coefficient parameter estimation uncertainty and Bayesian model evidence can also be estimated using closed form expressions. See [21] for details.

2.2 Estimation of the trim envelope

One important feature of the maneuverability model (9) is that it enables a rapid numerical analysis of the trimmable states. To see how this works first note the definition of the set of trimmable states is

$$\{\mathbf{x} | \mathbf{f}(\mathbf{x}, \mathbf{u}; \mathbf{c}) = 0, (\mathbf{x}, \mathbf{u}) \in \mathcal{B}\}, \quad (19)$$

where \mathcal{B} represents the set of overall allowable states and virtual inputs. This set is important because it represents an a-priori safe maneuverability envelope.

For the maneuverability model, and a given aerodynamic parameter vector \mathbf{c} , characterizing the set of trimmable points then involves setting the top and bottom equations on the right hand side of (9) equal to zero. The bottom equation is solved for angle of attack α in terms of the other variables in that equation, which do not include thrust T . The top equation is then solved for T into which the previous solution for α is substituted. The result is a closed form solution for the required thrust and alpha needed to achieve trim for any given trim state and other virtual inputs. This enables a fast numerical sweep to determine the non-convex trim envelope as follows:

1. Setup a grid of state values in \mathcal{B} . For most practical applications a coarse resolution is sufficient.
2. Fix values for roll angle ϕ and side-slip angle β , and make them equal to the current values.
3. For each point in the state grid solve for the thrust T and angle of attack α needed to achieve trim.
4. Return only those points for which T and α are within \mathcal{B} .

A crude visualization of the (V, γ) -trim envelope is then obtained by simply plotting the trimmable points from the above calculation. In addition, one should check whether the achieved trim points are stable. This involves checking the eigenvalues associated with the local linear approximation to (9) at each trim point, and as before a closed form expression can be found. The entire computation is fast enough

on a modern PC to enable dynamic re-computation as aircraft conditions change, or to compute extended envelopes by sweeping over values for ϕ and β .

The actual maneuverability calculation for a grid covering 5029 points is completed in 21 ms on a 2.6 GHz MacBook Pro. The calculation includes a check for stability[21]. An example trim envelope is shown in Fig. 3, and is based on the RCAM simulation model.

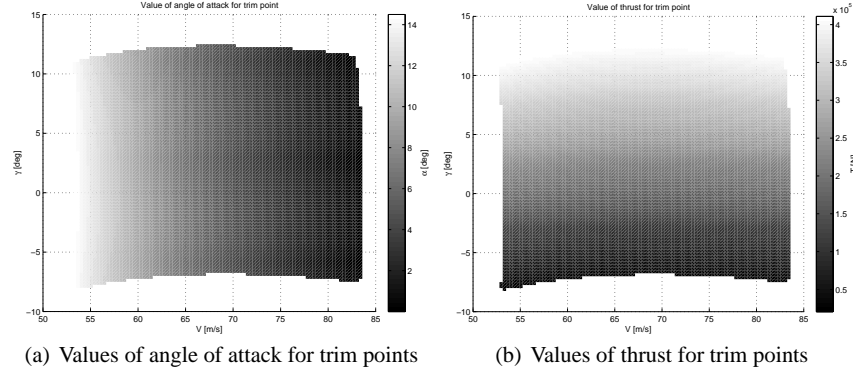


Fig. 3 Trim envelope for the RCAM model and required inputs for trim points

In Fig. 3, it can be seen that the trim envelope boundaries are imposed by the input saturation limits. The upper boundary corresponds to maximum thrust $T_{\max} = 410920\text{N}$, the lower boundary is imposed by minimum thrust $T_{\min} = 20546\text{N}$. The range for the angle of attack results in the boundaries left ($\alpha_{\max} = 14.5^\circ$, prior to stall) and right ($\alpha_{\min} = 0^\circ$). It can also be observed that more thrust is needed for larger flight path angles, because the thrust force has to counteract the exponentially increasing drag force, since a larger angle of attack occurs for slower speeds. Analyzing the range of thrust values over airspeed for constant flight path angle, shows that more thrust is needed for a further speed decrease below 69m/s . This region corresponds to the range of the angle of attack $\alpha > 4.5^\circ$. Analysis of the Lift-Drag Polar and the power required curve, shown in Fig. 4, confirms that this region is the back side of the power curve, and that $V = 69\text{m/s}$ is the minimum drag airspeed.

2.3 Estimation of the maneuvering envelope

In this context, the preferred interpretation of the safe maneuvering envelope considers reachability from the trim envelope. The stable and controllable trim envelope is considered an a-priori safe set. The backwards reachable set is defined as the set of states from where (at least one point in) the trim envelope can be reached. The forwards reachable set is defined as the set of states which can be reached from (at

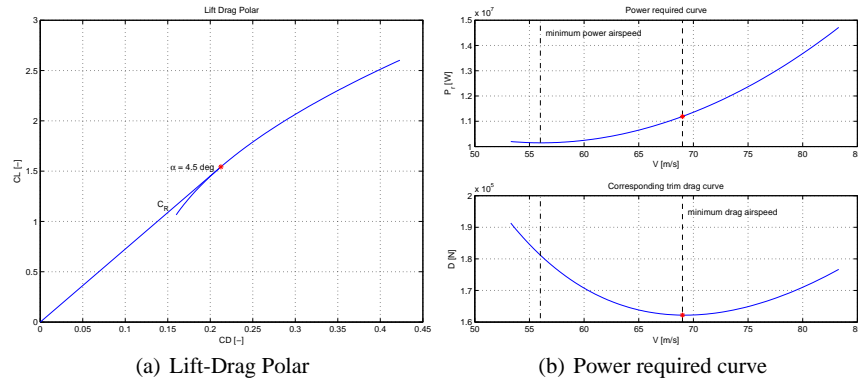


Fig. 4 Lift-Drag Polar and power required curve of the RCAM model confirm that minimum drag airspeed is $V = 69\text{m/s}$, and the region to the left is the back side of the power curve

least one point in) the trim envelope. Then the safe maneuvering flight envelope is the cross section between the forwards and backwards reachable sets. This interpretation is illustrated in Fig. 5. In addition to the safe envelope, the backwards reachable set is considered as the survivable flight envelope. After an upset due to damage, turbulence, a wake encounter etc., it is possible to bring the aircraft back to a safe trim condition as long as the current flight condition is situated inside the backwards reachable set.

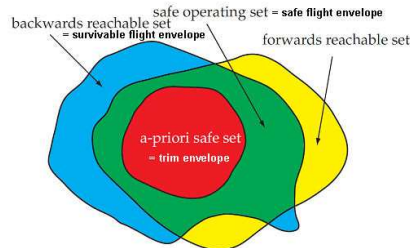


Fig. 5 Safe maneuvering envelope as intersection between forwards and backwards reachability, modified from source: van Oort[19]

The aim is to perform a combined forward and backward reachability analysis from the trim envelope as efficiently as possible, for on-line implementations. Based on previous research[4], level set methods are an excellent candidate. Finally, robustness is an important aspect to be considered in this context as well.

It has been shown in the literature that maneuvering envelope estimation through reachability can be reformulated in the optimal control framework[15]. Consider a continuous time control system:

$$\dot{\mathbf{x}} = \mathbf{f}(\mathbf{x}, \mathbf{u}, \Delta) \quad (20)$$

with $\mathbf{x} \in \mathbb{R}^n$, $\mathbf{u} \in U \subseteq \mathbb{R}^m$, $\Delta \in D \subseteq \mathbb{R}^k$, $\mathbf{f}(\cdot, \cdot) : \mathbb{R}^n \times U \rightarrow \mathbb{R}^n$, a function:

$$l(\cdot) : \mathbb{R}^n \rightarrow \mathbb{R} \quad (21)$$

and an arbitrary time horizon $T \geq 0$. Let $\mathcal{U}_{[t,t']}$ denote the set of Lebesgue and bounded measurable functions from the interval $[t, t']$ to U . Define $\phi(\tau, t, \mathbf{x}, \mathbf{u}(\cdot), \Delta)$ as the state trajectory. Δ are defined as parameter uncertainties. Given a set of states $K \subseteq \mathbb{R}^n$, the reachability question can be naturally formulated regarding the relation between the set K and the state trajectories ϕ of Eq. (20) over the horizon T . Problem of interest is the following:

Robust reachability: Does there exist a $\mathbf{u} \in \mathcal{U}_{[0,T]}$ and a $t \in [0, T]$ such that the trajectory ϕ of the state \mathbf{x} satisfies $\mathbf{x} \in K$, irrespective of Δ ?

The optimization problem can be formulated as a pursuit evasion game over the horizon $T \geq 0$ with target set $K \subseteq \mathbb{R}^n$ [5]. It is assumed that \mathbf{u} is trying to bring or keep the state in the set K , whereas Δ is trying to drive it out of K . To ensure the game is well-posed, \mathbf{u} is restricted to play non-anticipative strategies with respect to the unknown uncertainties Δ .

For the types of safety problems considered here, a set of initial states has to be established such that \mathbf{u} can win the game, in other words the set Reach can be characterized as follows:

$$\text{Reach}_{\text{robust}}(t, K) = \left\{ \mathbf{x} \in \mathbb{R}^n \mid \forall \Delta \in D, \exists \mathbf{u} \in \mathcal{U}_{[t,T]}, \right. \\ \left. \exists \tau \in [t, T], \phi(\tau, t, \mathbf{x}, \mathbf{u}(\cdot), \Delta) \in K \right\}$$

As done elsewhere in the literature[15], the characterization of this set can be done according to the principle of duality:

$$\text{Reach}(t, K) = (\text{Inv}(t, K^c))^c \quad (22)$$

Through this principle, it can be characterized as an INFMIN problem[15]. The crux is to include the Δ 's as disturbances in the optimization function, they oppose the optimization over \mathbf{u} . Consider a closed set K , that can be written as the level set of a continuous function $l : \mathbb{R}^n \rightarrow \mathbb{R}$, i.e. $K = \{\mathbf{x} \in \mathbb{R}^n \mid l(\mathbf{x}) \geq 0\}$. As a consequence, the Invariance optimization formulation becomes[5]:

$$\text{Inv}(t, K) = \{\mathbf{x} \in \mathbb{R}^n \mid V_2(\mathbf{x}, t) \geq 0\} \quad (23)$$

with:

$$V_2(\mathbf{x}, t) = \inf_{\mathbf{u}(\cdot) \in \mathcal{U}_{[t,T]}} \sup_{\Delta \in D} \min_{\tau \in [t,T]} l(\phi(\tau, t, \mathbf{x}, \mathbf{u}(\cdot), \Delta)) \quad (24)$$

This can be reformulated into an Hamilton-Jacobi-Bellmann Partial Differential Equation[15, 5]:

$$\frac{\partial V_2}{\partial t}(\mathbf{x}, t) + \min_{\tau \in [t, T]} \left\{ \inf_{\mathbf{u}(\cdot) \in \mathcal{U}_{[t, T]}} \sup_{\Delta \in D} \frac{\partial V_2}{\partial \mathbf{x}}(\mathbf{x}, t) \mathbf{f}(\mathbf{x}, \mathbf{u}, \Delta) \right\} = 0 \quad (25)$$

where $V_2(\mathbf{x}, T) = l(\mathbf{x})$ holds for backward integration and $V_2(\mathbf{x}, t) = l(\mathbf{x})$ applies to forward integration. These HJB PDE's can be solved by level sets, for which a toolbox is available in Matlab[®] [18].

A more elaborate discussion of the optimization strategy, and the detailed approach followed, is discussed by Lombaerts et al [12].

2.4 Maximum bank angle calculation

The maximum bank angle ϕ can be calculated as the bank angle at which the vertical component of the maximum attainable lift vector balances the weight vector of the aircraft. This means that banking the aircraft at the current airspeed beyond this maximum angle will result in a stall. This concept is illustrated in Fig. 6.

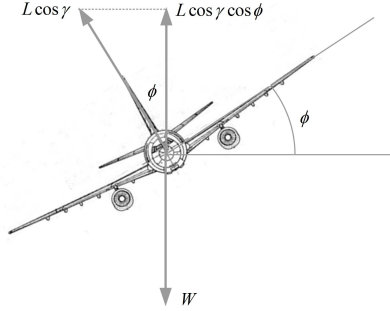


Fig. 6 Force balance between lift and weight in a turn

Equilibrium of forces in the vertical plane requires that:

$$L \cos \gamma \cos \phi = W \quad (26)$$

Rewriting for bank angle ϕ :

$$\cos \phi = \frac{W}{L \cos \gamma} = \frac{W}{C_L \frac{1}{2} \rho V^2 S \cos \gamma}, \quad (27)$$

For extreme bank angles the following relationship can be derived:

$$\cos \phi_{\max} = \frac{W}{L_{\max} \cos \gamma} = \frac{W}{C_{L_{\max}} \frac{1}{2} \rho V^2 S \cos \gamma}, \quad C_{L_{\max}} = C_{L_0} + C_{L_\alpha} \alpha_{\max} \quad (28)$$

Therefore, it can be stated that:

$$\pm\phi_{\max} = \pm \min \left\{ \arccos \left(\frac{W}{C_{L_{\max}} \frac{1}{2}\rho V^2 S \cos \gamma} \right), 35^\circ \right\} \quad (29)$$

where $C_{L_{\max}} = C_{L_0} + C_{L_\alpha} \alpha_{\max}$. In this calculation the current values for airspeed V and flight path angle γ are used, the up-to-date values for C_{L_0} and C_{L_α} as provided by the identification algorithm, as well as the maximum angle of attack α_{\max} . For normal maneuvers of a conventional civil airliner, the maximum bank angle is not expected to exceed 35° .

Reducing speed will restrict the available bank range to lower values of $\pm\phi_{\max}$. At stall speed, no bank authority will be left. Some typical values for the nominal RCAM model are given in Table 2.

Table 2 Some typical values of maximum bank angle at different airspeeds for the RCAM model

V [m/s]	α [°]	ϕ_{\max} [°]
75	3	± 60
59	9	± 35
53	14.5	≈ 0

3 Additional information provided to the pilot over the cockpit displays

The information obtained from the envelope estimation algorithm can then be presented to the pilot. This is done in the primary flight display (PFD). The speed and flight path angle boundaries, which apply for the current bank angle and sideslip angle, are shown on the relevant parts of the PFD. Also the bank angle limits are displayed on the PFD.

The calculated true airspeed boundaries (TAS) are converted to indicated airspeed (IAS) by taking into account altitude varying air density and presented on the speedtape at the left hand side of the artificial horizon in the PFD. The flight path angle information γ is translated into vertical speed \dot{h} and presented on the vertical speed tape at the right hand side of the artificial horizon in the PFD.

Safe envelope information presented on the vertical speed tape, as illustrated in Fig. 7, is absent in current PFDs. In this new setup, the amber lines mark the vertical speed ranges where no equilibrium can be established. In practice, this means that speed will increase in the lower amber region, even for idle thrust, and that speed will decrease in the upper amber region, even with full thrust. The red barber poles mark the ranges where the maneuverability envelope is left. In practice, this means that it is impossible to reach this range and return to trim within 5 s for each direction. For the bank angle limits, the amber region is static on the 35° marker. The red

barber regions indicate where stall will occur and are determined by the maximum bank angle as calculated in Sec. 2.4.

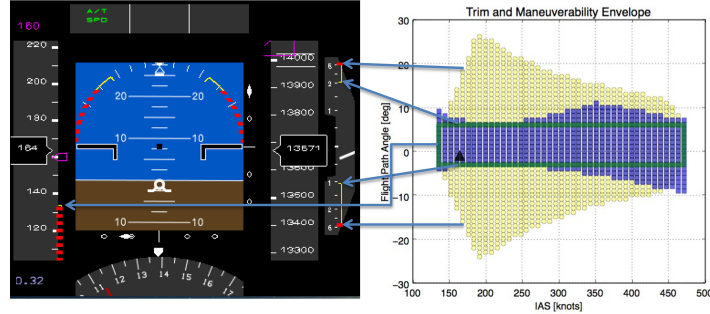


Fig. 7 The envelope limits as displayed on the primary flight display, and how they are driven by the envelope calculation

4 Application examples

Two main application examples have been considered in this research, both scenarios have an impact on the speed boundaries of the safe flight envelope. The first one is a generic simplified icing scenario, the latter is an unscheduled stabilizer deflection. The nature of both scenarios is elaborated in detail, after which the calculated effects on the envelope are analysed. Finally the observations are verified from a flight dynamics point of view.

4.1 Icing scenario

In specific atmospheric conditions, ice accretion is possible on the aircraft wings. In this example, it is assumed that the regular thermal anti-ice systems, which are conventional equipment on all civil airliners, are operating but are not successful in removing all and/or preventing any ice being built up on the wings. This example will focus on the impact of ice accretion on the flight performance envelope of the aircraft.

4.1.1 Impact on the simulation model

The influence of icing can be injected into the maneuverability model through two primary mechanisms. First, changes in the flight dynamics are represented through the aerodynamic parameters. Typically, icing will decrease lift C_L and increase drag C_D . For this simplified example, all lift coefficients (C_{L_0} and C_{L_α}) have been scaled down by 20%, and all drag coefficients (C_{D_0} , C_{D_α} and $C_{D_{\alpha^2}}$) up by 20%. The second mechanism is modeling diminished control authority through the set \mathcal{B} of overall allowable virtual inputs. For example, the maximum permissible angle of attack may diminish due to icing. In this generic example, the stall angle of attack α_{\max} is reduced from 14.5° to 8° , in addition to the coefficient changes, and its impact on the safe flight envelope has been analysed.

4.1.2 Effect on the safe flight envelope

Fig. 8(a) shows that a 20% decrease in lift combined with a 20% increase in drag results in a shift of the trim envelope towards higher airspeeds and lower flight path angles. The following force equilibrium equations explain this physically:

$$C_L(\alpha) \frac{1}{2} \rho V^2 S = W \cos \gamma \approx W \quad (30)$$

$$T - C_D(\alpha) \frac{1}{2} \rho V^2 S = W \sin \gamma \approx W \gamma \quad (31)$$

Due to the reduced lift capability, it can be seen in Eq. 30 that a higher airspeed is needed to compensate for the aircraft weight. On the other hand, an increase in drag means that less net excess thrust is available for climb in Eq. 31. If the maximum angle of attack limit α_{\max} is reduced, then there is a further reduction in maximum lift capability, which is translated into a shift to the right of the left limit of the trim envelope, as shown in Fig. 8(b). Note that a decrease in α_{\max} leads to the loss of any possibility to establish trim below approximately $V = 70\text{m/s}$.

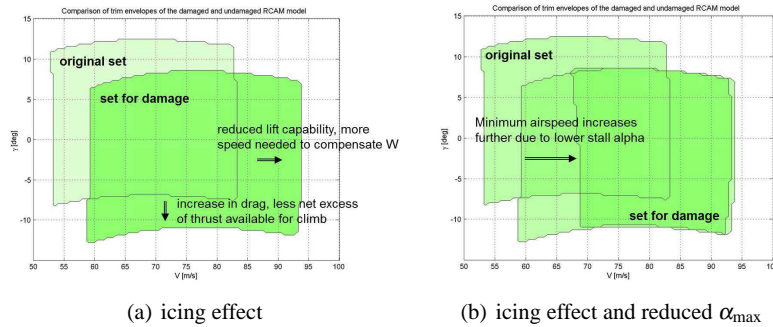


Fig. 8 Comparison of trim envelopes of the damaged and undamaged RCAM model

Next the V, γ maneuvering envelope is calculated for bank angle $\phi = 0$, with and without generic icing scenario involving 20% decrease in lift force and increase in drag force, and with an additional envelope degradation scenario caused by a reduced maximum angle of attack. This example builds further on the results for the trim envelope, as presented in Fig. 8. The intersection of forwards and backwards reachability is defined as the safe maneuvering envelope and is shown in Fig. 9. The time horizon in this example is set at $T = 5$ s. This choice is based on the time constants of the considered relevant dynamics. The blue rectangular contour corresponds to the rectangle with the largest area which can be drawn in the trim envelope of the nominal aircraft as depicted in Fig. 3. Similarly the red contours correspond to the rectangles with the largest area which can be spanned in the trim envelopes of both damage scenarios in Fig. 8(b).

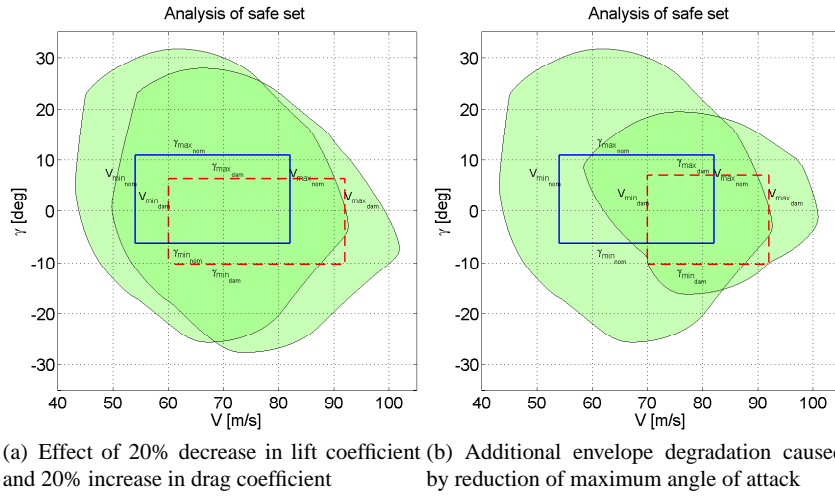


Fig. 9 Calculation of safe maneuvering envelope sets through forward and backward reachability analysis over $T = 5$ s, based on calculated trim envelope boundaries and identified aerodynamic parameters. Upper left envelope areas correspond to nominal configuration.

Comparing undamaged and damaged envelope boundaries shows the influence of the damage characteristics. In Fig. 9(a), it can be seen that the safe maneuvering envelope shift is similar as for the trim envelope. A higher speed range is needed to compensate for the loss in the lift force coefficient, and not as large positive flight path angles can be reached due to the smaller excess of net thrust due to the increased drag. In Fig. 9(b), it can be seen that the restriction on maximum angle of attack leads to a further shrinking of the maneuvering envelope, especially for slower speeds since stall will occur for higher airspeeds.

Extensive Monte Carlo analyses have been performed in order to verify the accuracy of the boundaries of the estimated maneuvering envelopes. These analyses have been based on the non-simplified aircraft model, ignoring the assumption that the

aerodynamic angles α and β should be small. All these Monte Carlo analyses have confirmed that the results provided here are accurate and that the simplifications hold for the current ranges of the aerodynamic angles, namely $\alpha \in [0^\circ; 14.5^\circ]$ (no icing) and $\beta \in [-5^\circ; +5^\circ]$. This is an important conclusion which makes a relevant on-line safe maneuvering envelope estimation tool much more feasible.

4.1.3 Maximum bank angle in icing conditions

Since the total maximum lift capability $C_{L_{\max}}$ of the aircraft characteristics will decrease in an icing scenario, while the total weight W will remain unchanged, it can be expected that this will have a significant impact on the maximum bank angle. As a consequence $\cos \phi_{\max}$ will increase, which corresponds to a decrease in ϕ_{\max} . The effect and comparison without icing is shown in table 3.

Table 3 Some typical values of maximum bank angle at different airspeeds for the RCAM model with and without icing

V [m/s]	84	75	66	59	53
$\phi_{\max} [^\circ]$ with ice	± 60	± 50	± 35	≈ 0	0
$\phi_{\max} [^\circ]$ no ice	± 66	± 60	± 49	± 35	≈ 0

4.2 Stabilizer misalignment

Another scenario considered in this study, was a nose down stab trim misalignment, which generates a pitch up moment. The disturbing moment must then be counteracted by the elevators, which come close to their saturation limits. This results in significantly stricter upper envelope limits on speed and climb rate. For practical purposes, it is important to achieve zero angular rates around all body axes, in order to establish a stabilized final approach. Relying on Newton's second law for rotations: $\mathbf{M}_\alpha = \mathbf{I}\dot{\boldsymbol{\omega}} + \boldsymbol{\omega} \times \mathbf{I}\boldsymbol{\omega}$, the requirement for $\boldsymbol{\omega} = 0$ as well as $\dot{\boldsymbol{\omega}} = 0$, results in the requirement that the total aerodynamic moment \mathbf{M}_α (the pitching moment M around the Y-axis in the specific case considered here) should be equal to zero.

Considering Eq. (10) for this specific case:

$$C_m = 0 = C_{m_0} + C_{m_\alpha} \alpha + \underbrace{C_{m_q} \frac{q\bar{c}}{V}}_{q=0} + C_{m_{\delta_e}} \delta_e + \underbrace{C_{m_{i_h}} i_h}_{\text{disturbance}} + C_{m_T} \frac{T}{\bar{q}d_{\text{eng}}^2} \quad (32)$$

for the combination of the required pitch rate $q = 0$ and the disturbance i_h caused by the misaligned stab, together with the given trim values for angle of attack α and thrust T calculated earlier, a specific value for elevator deflection δ_e is needed in order to balance the total Eq. (32), while taking into account the upper saturation

limit of the elevator $\delta_{e_{\max}}$. Eq. (32) is an additional trim requirement, besides Eq. (9). In most conventional flight conditions without stab misalignment, Eq. (32) has no effect on the shape of the trim envelope. However, the impact on the trim envelope is significant for large angle stabilizer misalignment, as can be seen in Fig. 10.

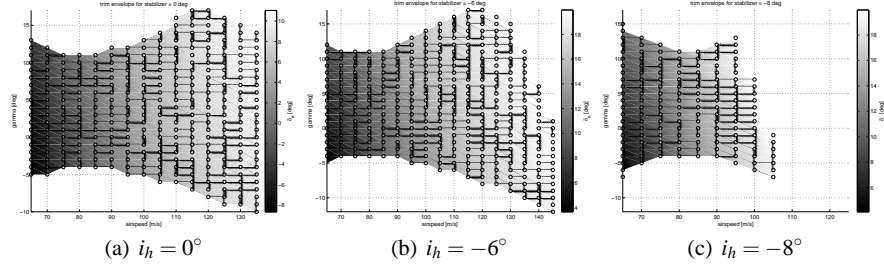


Fig. 10 V, γ trim envelopes for different stabilizer misalignment scenarios for bank angle $\varphi = 0$ and sideslip angle $\beta = 0$. Elevator saturation limits are -30° and $+20^\circ$.

Fig. 10(a) shows that the required elevator deflections for a stabilizer stuck at 0° vary between -8° and 15° over the entire trim envelope, which is well between the elevator saturation limits -30° and $+20^\circ$. However, Fig. 10(b) and 10(c) show a totally different situation for a stabilizer misalignment at 6° or 8° nose down respectively. The pitch up moment which is generated requires significant elevator deflection and they hit their maximum limit at $\delta_{e_{\max}} = 20^\circ$ within the trim envelope calculated based on lift and drag. This additional input constraint results in the fact that the envelope is significantly smaller. For level flight $\gamma = 0^\circ$, the conventional maximum airspeed of $V = 135\text{m/s}$ is reduced to $V = 100\text{m/s}$ for $i_h = -8^\circ$ to prevent elevator saturation. This is relevant information, which increases the crew's situational awareness significantly in this type of scenario.

5 Conclusions and recommendations

The methods presented in this paper have three distinguishing features. First, instead of linearizing the full aircraft dynamics model, a representative compact nonlinear model has been determined. This enabled rapid numerical computations, which are more representative of the aircraft performance than would be obtained through linearized models. Second, the integrated modular approach involving system identification – trim envelope calculation – maneuvering envelope calculation leverages the same dynamics model to estimate the safe flight envelope from currently available flight data as provided by current sensor packages on-board civil airliners, while also establishing confidence regions biased towards greater uncertainty when insufficient input excitation is available. Furthermore, the system identification process makes the global approach adaptive for (unintentional) configuration changes and damage,

which has been shown in the application examples. Third, the safe maneuvering envelope maximizes the options pilots or automation systems have to recover the aircraft in damage scenarios, while remaining robust to the uncertainty in the system identification process. The net result is an increased flexibility for developing advanced aircraft diagnostics that provide the bottom line maneuverability of the aircraft as an output, and this is expected to have important applications to flight planning, trajectory generation, guidance algorithms, and pilot displays.

6 Further research

The display features presented here, providing up to date safe flight envelope information to the flight crew, have been evaluated in the Advanced Concepts Flight Simulator at NASA Ames Research Center to investigate the impact on aircraft energy state awareness of the crew. Commercial airline crews have flown multiple challenging approach and landing scenarios in a relevant environment simulating the airspace around Memphis International Airport. More details and extensive results of this specific simulator study can be found in Ref. [11].

Acknowledgements This work is supported by NASA's Aviation Safety Program, through the Vehicle Systems Safety Technologies (VSST) project, and by a Marie Curie International Outgoing Fellowship (IOF) within the 7th European Community Framework Program.

References

1. Statistical summary of commercial jet airplane accidents – worldwide operations 1959 - 2011. Technical report, Boeing Commercial Aircraft, July 2012. Available at: <http://www.boeing.com/news/techissues/pdf/statsum.pdf>.
2. Cast safety enhancement plan. Technical Report SE207, Commercial Aviation Safety Team, 2013. Available at: www.skybrary.aero/index.php/Portal:CAST_SE_Plan.
3. Barton J. Bacon. Quaternion based control architecture for determining controllability/maneuverability limits. In *Guidance, Navigation, and Control and Co-located Conferences*, number AIAA 2012-5028. American Institute of Aeronautics and Astronautics, aug 2012.
4. Nithin Govindarajan. An optimal control approach for estimating aircraft command margin – with applications to loss-of-control prevention. Masters thesis, Delft University of Technology, October 2012. Available at: <http://repository.tudelft.nl/view/ir/uuid%3A48dbad61-728a-4c7e-ba3e-cf8382ef1cef/>.
5. Ioannis Kitsios and John Lygeros. Launch pad abort flight envelope computation for a personnel launch vehicle using reachability. In *AIAA Guidance, Control and Navigation*, number AIAA 2005-6150, August 2005.
6. Herman J. Koolstra, Herman J. Damveld, and Jan Albert Mulder. Envelope determination of damaged aircraft. In *Guidance, Navigation, and Control and Co-located Conferences*, number AIAA 2012-4699. American Institute of Aeronautics and Astronautics, aug 2012.

7. Harry G. Kwatny and Robert C. Allen. Safe set maneuverability of impaired aircraft. In *Guidance, Navigation, and Control and Co-located Conferences*, number AIAA 2012-4405. American Institute of Aeronautics and Astronautics, aug 2012.
8. Matthew D. Lichter, Alec J. Bateman, and Gary Balas. Flight test evaluation of a run-time stability margin estimation tool. In *AIAA Guidance, Navigation and Control Conference*, number AIAA 2009-6257, August 2009.
9. Thomas Lombaerts. *Fault Tolerant Flight Control – A Physical Model Approach*. Phd dissertation, Delft University of Technology, May 2010. Available at: <http://repository.tudelft.nl/view/ir/uuid%3A538b0174-fe84-43af-954d-02f256b2ec50/>.
10. Thomas Lombaerts, Eddy Van Oort, Qiping Chu, Jan Albert Mulder, and Diederick Joosten. On-line aerodynamic model structure selection and parameter estimation for fault tolerant control. *Journal of Guidance, Control and Dynamics*, 33(3):707–723, May–June 2010.
11. Thomas Lombaerts, Stefan Schuet, Diana Acosta, John Kaneshige, Kimberlee Shish, and Lynne Martin. Piloted simulator evaluation of maneuvering envelope information for flight crew awareness. In *AIAA GNC Conference*, number AIAA-2015-1546, January 2015.
12. Thomas Lombaerts, Stefan Schuet, Kevin Wheeler, Diana Acosta, and John Kaneshige. Safe maneuvering envelope estimation based on a physical approach. In *AIAA Guidance, Navigation and Control (GNC) Conference*, number AIAA-2013-4618, August 2013.
13. T.J.J. Lombaerts, Q.P. Chu, J.A. Mulder, and D.A. Joosten. Real time damaged aircraft model identification for reconfiguring control. In *Proceedings of the AIAA AFM Conference and Exhibit*, number AIAA-2007-6717, August 2007.
14. Gertjan Looye and Samir Bennani. Description and analysis of the research civil aircraft model (rcam). Technical report TP-088-27, Group for Aeronautical Research and Technology in Europe GARTEUR, 1997.
15. John Lygeros. On reachability and minimum cost optimal control. *Automatica*, 40:917–927, 2004.
16. Padmanabhan Menon, Jinwhan Kim, Prasenjit Sengupta, Veera Vaddi, Bong-Jun Yang, and Jason Kwan. Onboard estimation of impaired aircraft performance envelope. In *Guidance, Navigation, and Control and Co-located Conferences*, number AIAA 2011-6688. American Institute of Aeronautics and Astronautics, aug 2011.
17. N. Meuleau, C. Neukom, C. Plaunt, D. Smith, and T. Smith. The emergency landing planner experiment. In *ICAPS-11 Scheduling and Planning Applications Workshop*, 2011.
18. Ian M. Mitchell. The flexible, extensible and efficient toolbox of level set methods. *journal of Scientific Computing*, 35:300–329, 2008.
19. Eddy Van Oort, Ping Chu, and Jan Albert Mulder. *Advances in Aerospace Guidance, Navigation and Control*, chapter Maneuvering Envelope Determination through Reachability Analysis, pages 91–102. Springer - Verlag, 2011.
20. Rohit Pandita, Abhijit Chakraborty, Peter Seiler, and Gary Balas. Reachability and region of attraction analysis applied to gtm dynamic flight envelope assessment. In *AIAA Guidance, Navigation and Control Conference*, number AIAA 2009-6258, August 2009.
21. Stefan Schuet, Thomas Lombaerts, Diana Acosta, Kevin Wheeler, and John Kaneshige. An adaptive nonlinear aircraft maneuvering envelope estimation approach for online applications. In *AIAA SciTech Guidance, Navigation and Control (GNC) Conference*, number AIAA 2014-0268, January 2014.
22. Jong-Yeob Shin and Christine Belcastro. Robustness analysis and reliable flight regime estimation of an integrated resilient control system for a transport aircraft. In *AIAA Guidance, Navigation and Control Conference*, number AIAA 2008-6656, August 2008.
23. Liang Tang, Michael Roemer, Sudarshan Bharadwaj, and Christine Belcastro. An integrated health assessment and fault contingency management system for aircraft. In *AIAA Guidance, Navigation and Control Conference*, number AIAA 2008-6505, August 2008.
24. James M. Urnes, Eric Y. Reichenbach, and Timothy A. Smith. Dynamic flight envelope assessment and prediction. In *AIAA Guidance Navigation and Control Conference*, number AIAA 2008-6983, August 2008.